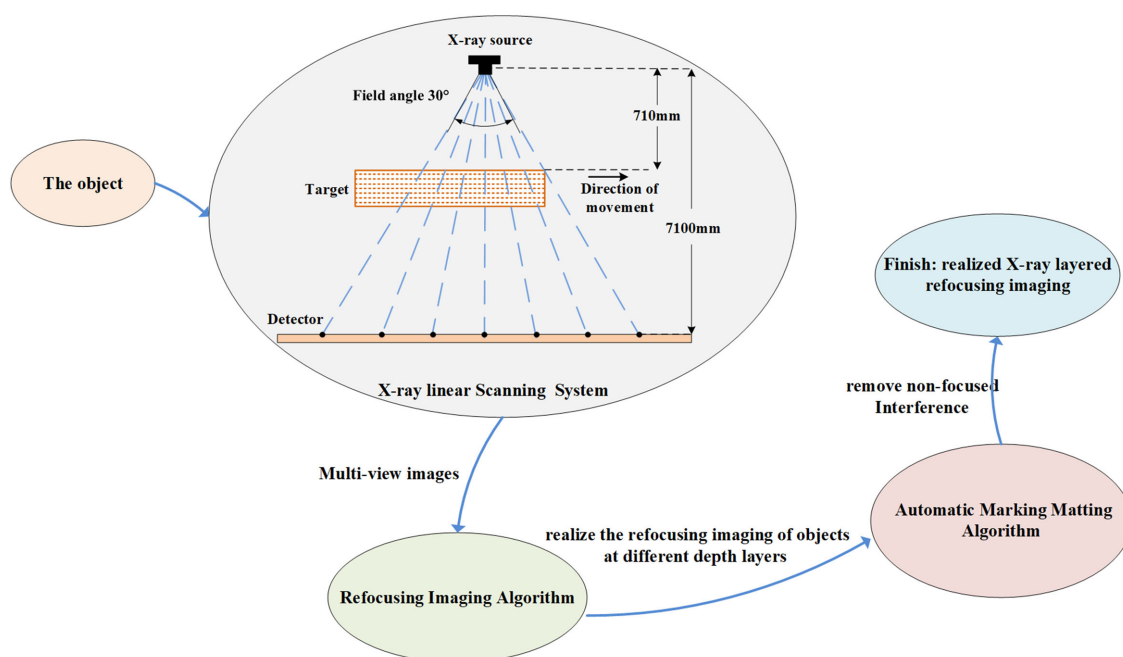


X-Ray Layered Refocusing Imaging Based on Linear Scanning


Volume 12, Number 3, June 2020

Bin Liu
Yue Luo
Ke Li
Xia Zhao



DOI: 10.1109/JPHOT.2020.2998916

X-Ray Layered Refocusing Imaging Based on Linear Scanning

Bin Liu,^{1,2} Yue Luo ,^{1,2} Ke Li,^{1,2} and Xia Zhao^{1,2}

¹School of Information and Communication Engineering, North University of China, Taiyuan 030051, China

²National Defense Technology Key Laboratory of Electronic Testing Technology, Taiyuan 030051, China

DOI:10.1109/JPHOT.2020.2998916

This work is licensed under a Creative Commons Attribution 4.0 License. For more information, see <https://creativecommons.org/licenses/by/4.0/>

Manuscript received April 16, 2020; revised May 17, 2020; accepted May 26, 2020. Date of publication June 1, 2020; date of current version June 12, 2020. This work was supported in part by the National Natural Science Foundation of China under Grant 61971381. Corresponding author: Xia Zhao (e-mail: zhaoxia0316@nuc.edu.cn).

Abstract: In the process of X-ray digital imaging, due to the mutual occlusion of object structures of different depth layers, the image projection information is overlapped. X-CT(Computed-Tomography) and X-CL(Computed-Laminography) are usually used to obtain structural information of objects at different depths, but they are limited by accurate multi-dimensional motion control systems, complex scanning methods and poor real-time computing performance. To solve the problems, this paper proposed a method of X-ray layered imaging based on linear scanning. This method only needs the object to pass through the detection area along a straight line to realize the multi-view imaging, extracts the effective multi-view images information for refocusing imaging, and realizes the reconstruction of different depth layers of the object. Meanwhile, the automatic marking matting algorithm is employed to remove the non-focused interference in the refocused images. Experiments of X-ray layered imaging were conducted, which demonstrated the proposed method can achieve objects reconstruction with different depths, and effectively remove the non-focused interference.

Index Terms: X-ray, linear scanning, refocusing imaging, automatic marking matting algorithm.

1. Introduction

With the development of X-ray detector and digital image processing techniques, X-ray imaging detection technology has been widely used as one of the conventional non-destructive testing techniques. Due to the principle of X-ray imaging, there is a lack of three-dimensional structure information in single-view X-ray projection images [1], [2]. In order to obtain structural information of objects at different depth layers, X-CT and X-CL are usually used [3], [4]. Although the imaging techniques of X-CT and X-CL can achieve high accuracy, they are limited by accurate multi-dimensional motion control systems, and poor real-time computing performance [5]. such as detecting and identifying the objects occluded by metal in luggage security inspection, Neither of the two can quickly achieve clear imaging of objects at different depths, which is not conducive to real-time detection in simple occasions such as X-ray security check and industrial defect detection.

In view of the above questions, in order to achieve clear imaging of objects at different depths and maintain high real-time computing performance, this paper studies the X-ray layered refocusing

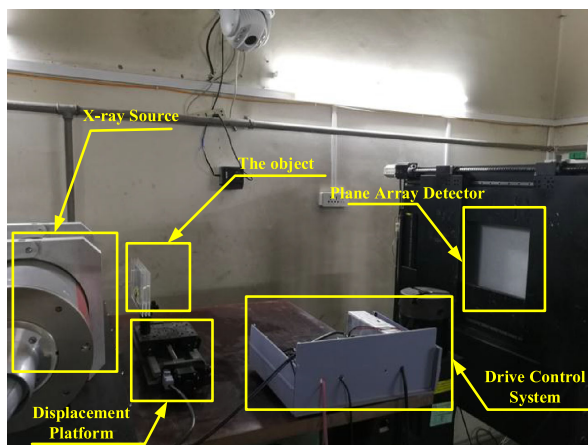


Fig. 1. X-ray linear scanning system.

imaging method: Section 2 introduces the related works at home and abroad. Section 3.1 proposes a multi-view imaging system based on X-ray linear scanning. Section 3.2 extracts the effective multi-view images information and uses the light field refocusing algorithm [6]–[8] to realize the refocusing imaging of objects at different depth layers. Section 3.3 improves the traditional matting algorithm of manually marking trimap, and proposes a method for automatically marking the trimap, which can effectively and rapidly remove the non-focused interference in the refocused image. Section 3.4 carries out a simulation experiment. Section 4 presents the experimental results and discussion. Section 5 summarizes the research.

2. Related Work

CT imaging technology is often used to reconstruct the objects at different depth layers, but the complex scanning method and reconstruction algorithm make the reconstruction more time-consuming [9]–[11]. In the linear scanning method of CL imaging technology, a reverse movement of the ray source and the object can achieve only a clear imaging of the specified depth layer of the detected object. To obtain structural information of the object at different depth layers, multiple reverse movements are required [12], [13]. Therefore, X-CT and X-CL can not achieve simple application requirements.

At present, in the field of visible light, camera array is usually used to multi-view imaging of the object. The refocusing algorithm can achieve the refocusing imaging of different depth layers of the object by using multi-view images [14], [15]. Since the refocused image not only contains object information in the focused area, but also interference information in the non-focused area. In 2005, Wilburn B *et al.* used dynamic labeling method to remove the interference information [16]. In 2013, P. Zhao *et al.* used the minimum energy method to remove interference [17]. In 2010, J. Zhu *et al.* proposed a matting method of manually marking trimap [18] to separate the object and interference information.

3. X-Ray Layered Refocusing Imaging Based on Linear Scanning

3.1 Multi-View Imaging System Based on X-Ray Linear Scanning

The X-ray linear scanning system designed in this paper uses the plane array detector, which collects the different angle information of the object moving at a constant speed on a high-precision displacement platform. In the experiment, the movement of the object is controlled by controlling the movement of the displacement platform, and the specified detector line is extracted from the

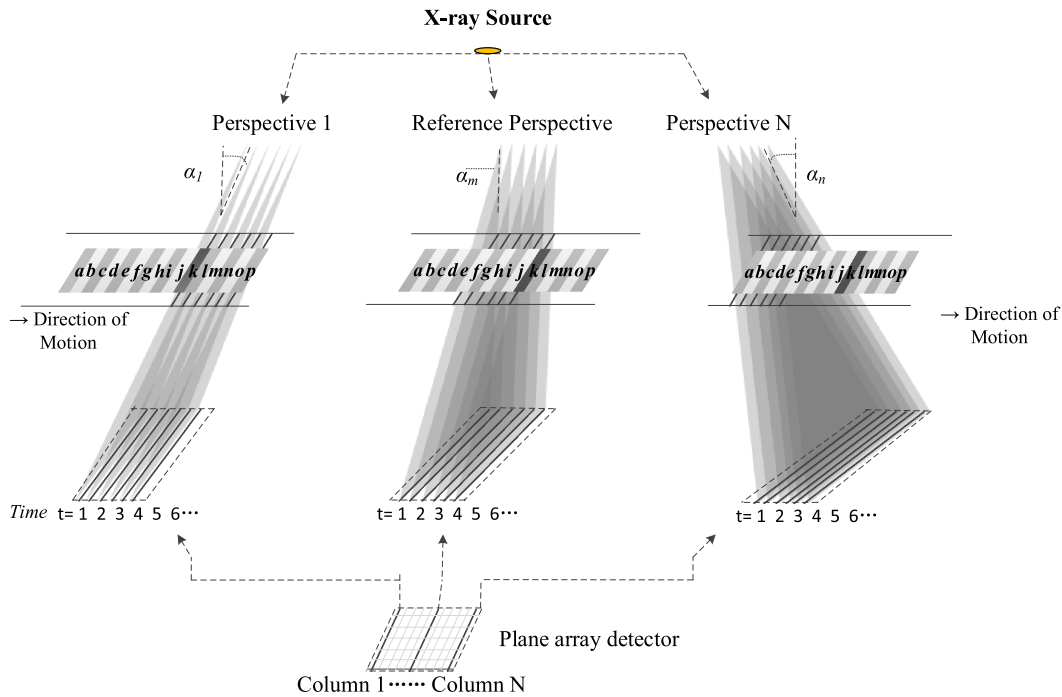


Fig. 2. Acquisition process of multi-view images.

plane array detector to obtain the multi-view projection images of the object. Fig. 1 is the picture of the system.

Because the positions of the X-ray source and the detector are fixed, the field-of-view covered by the X-ray source is unchanged. The deflection angle between each detector line and the central axis of the system is α_j , and X-ray scans the object at different angles α_j . Fig. 2 shows the acquisition process of multi-view images. This paper only explains the process from three perspectives: α_1 , α_m and α_n . The object in Fig. 2 is a writing board, the different positions on the writing board is identified by letters, from left to right are the letters $a \sim p$. The high-precision displacement platform moves uniformly from left to right.

The detector gets the object information from different angles α_j to form multi-view images. For example, the detector line under perspective α_1 obtains the information of region k at time $t = 1$, while the detector line under reference perspective α_m obtains the information of region k at time $t = 6$, and the detector line under perspective α_n obtains the information of region k after multiple moments. Since the writing board moves with the displacement platform at a constant speed, different angle information of region k can be obtained from different perspectives α_j , that is, multi-view information of region k . With the passage of time, the detector line under the perspective α_1 can obtain the complete information of region $a \sim p$ in a certain period. Similarly, the detector line under the perspective α_m and the perspective α_n can also obtain the complete information of region $a \sim p$. At this time, images obtains from different perspectives α_j are multi-view images of the object.

The system described above is used to collect the multi-view images of the object, and the collected images are shown in Fig. 3.

3.2 Refocusing Imaging Algorithm

In this paper, the light field refocusing technology is applied to the multi-view images obtained by X-ray linear scanning to realize the refocusing imaging of the objects at different depth layers.

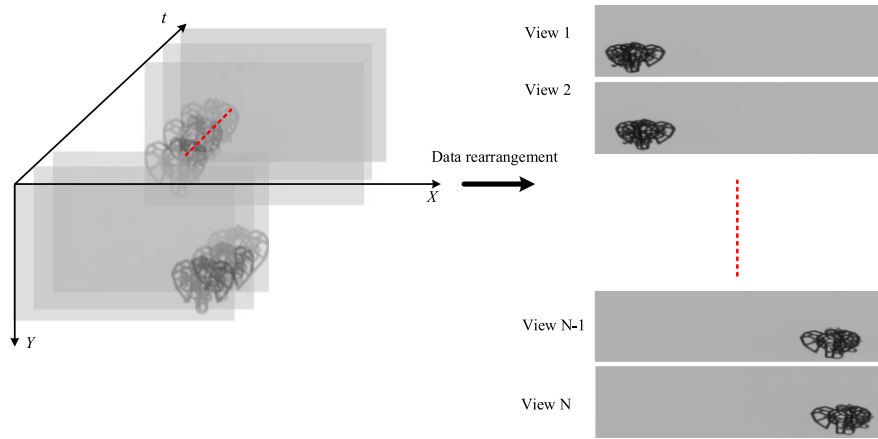


Fig. 3. Multi-view projection images based on X-ray linear scanning system.

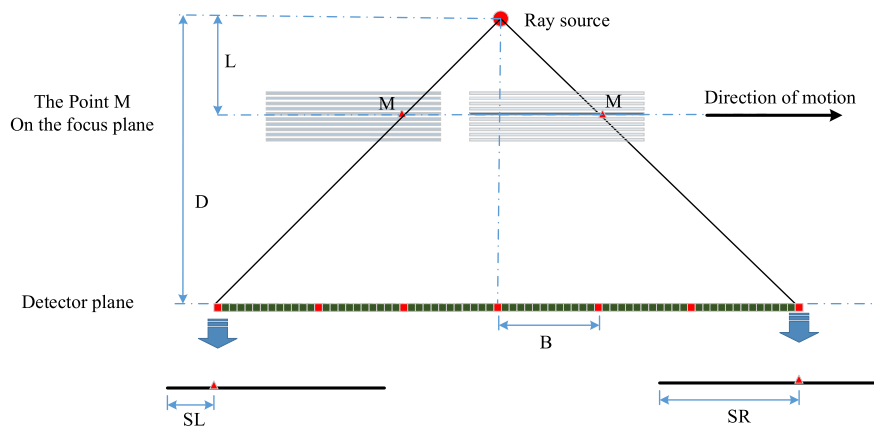


Fig. 4. Schematic diagram of X-ray layered refocusing imaging system.

The main idea of the refocusing algorithm [14]–[16] is that the refocused image of the specified object plane can be obtained by performing a panning operation (de-parallax) on each view projection image and averaging the de-parallax multi-view projection images. Therefore, it is necessary to calculate the parallax of multi-view images at the specified focused object plane, and the parallax analysis is shown in Fig. 4.

As shown in Fig. 4, the object point M at a specific depth has a distance L between the ray source and object plane, which is in the range of $L_{\min} \leq L \leq L_{\max}$ since the object has a certain thickness. The distance between the ray-source and the plane where the detector is located is D , and N columns of the array detector are extracted to realize multi-view imaging. The distance between each column of sensors is B . Assuming that the pixel size of detector is Δd , the step of moving the object is d_{step} . The sampling frequency of the detector should be matched with the object moving speed to ensure the integrity of object information, that is,

$$d_{step} = \frac{L_{\min}}{D} \cdot \Delta d. \quad (1)$$

For the examples of the left and right detector columns, the projection positions of point M from the begin-end in the corresponding two projection images are SL and SR , respectively. Therefore,

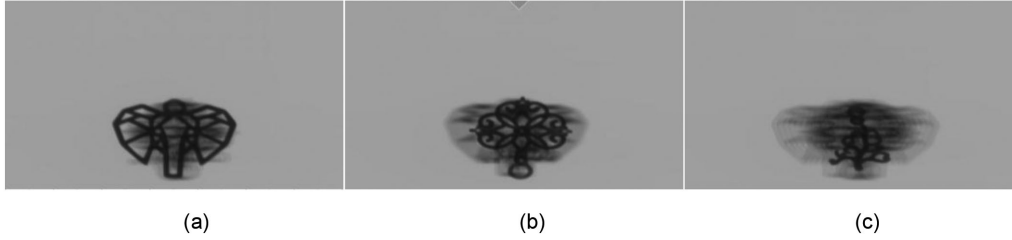


Fig. 5. Refocusing results at different layers. (a) Refocus on the foreground layer. (b) Refocus on the middle layer. (c) Refocus on the background layer.

the parallax formed in the two-view projections is: $\Delta s = SR - SL$ (the parallax is measured in the number of pixels).

Since the moving step of point M is d_{step} , according to the triangular geometric relationship, the corresponding imaging step $\Delta d'$ in the detector is: $\Delta d' = \frac{D}{L} d_{step} = \frac{L_{min}}{L} \Delta d$, where L_{min} refers to the distance from the front end of the object to the X-ray source.

Then, since the distance between the leftmost and rightmost detector columns is $(N - 1) \cdot B$, the parallax of point M in the image collected by the two detector columns is

$$\Delta s = \frac{(N - 1) \cdot B}{\Delta d'} = \frac{(N - 1) \cdot B \cdot L}{L_{min} \Delta d} \quad (2)$$

Based on the principle of multi-view refocusing, a central reference view $N_r (1 \leq N_r \leq N)$ is required to be selected in the X-ray multi-view projection refocusing process. Assuming that the point M is located at the focused object plane, the parallax generated by each view n relative to the reference view can be expressed as

$$\Delta s_{n,L} = \begin{cases} \frac{(N_n - N_r) \cdot B \cdot L}{L_{min} \cdot \Delta d} & (n > r) \\ \frac{(N_r - N_n) \cdot B \cdot L}{L_{min} \cdot \Delta d} & (n < r) \end{cases} \quad (3)$$

Assuming that s is the coordinates of a point on the multi-view image, and s' is the coordinates of a point on the parallax removed multi-view image, α is the focus coefficient, $I_{n,L}(s)$ is the multi-view image captured by perspective n focusing on a specified depth layer L . With the parallax $\Delta s_{n,L}$ calculated above, the parallax removed multi-view image $I_{n,L}(s')$ can be expressed as

$$I_{n,L}(s') = I_{n,L}(s + \Delta s_{n,L} + \alpha \cdot B) \quad (4)$$

The refocused image S_L , which focuses on the specified depth layer L can be obtained by performing an averaging operation as follows

$$S_L = \frac{1}{N} \sum_{n=1}^N I_{n,L}(s') \quad (5)$$

Moreover, the object reconstruction at different depth layers L can be also achieved by setting a focus coefficient α after acquiring multi-view images, and the refocusing imaging results at different layers are shown in Fig. 5.

3.3 Automatic Marking Matting Algorithm of Removing Non-Focused Interference

As shown in Fig. 5, the refocusing imaging can effectively enhance the structural information of the under-reconstructed objects, while a large interference caused by under-reconstructed objects during the refocusing imaging process. Among them, the under-reconstructed objects refer to the focused objects and the non-reconstructed objects refer to the non-focused interference.

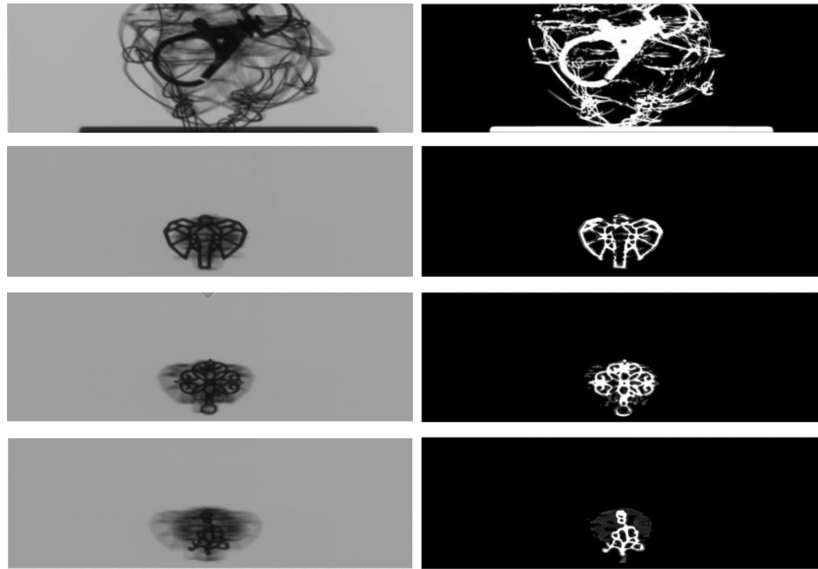


Fig. 6. The results of automatically marking the trimap.

Image matting can effectively separate the object and interference information in the image, this paper improved the image matting algorithm of manually marking trimap [18], and proposed a method of automatically marking the trimap, so as to automatically determine the regions that need to be reserved and deleted.

According to the refocusing principle: for the object on the focused position, the pixel values of the parallax removed multi-view images are basically the same as those of the center reference view image, so the refocused image at this position is clear, while for the object on the non-focused position, the pixel values of the parallax removed multi-view images are quite different from those of the center reference view image, so the refocused image at this position is blurred. Through this principle, we can judge the focusing degree of the pixels in the refocused image, the focusing degree evaluation function is defined as

$$C(x, y) = \frac{1}{N} \sqrt{\sum_{n=1}^N [I_{n,L}(x, y) - S_L(x, y)]^2} \quad (6)$$

where, $S_L(x, y)$ is the refocused image, $I_{n,L}(x, y)$ is the parallax removed multi-view image, and N is the number of viewpoints. It can be seen that the smaller the value of $C(x, y)$ is, the clearer the refocused image is at the pixel (x, y) ; the larger the value of $C(x, y)$ is, the more blurred the refocused image is at the pixel (x, y) . By setting the threshold values for $C(x, y)$, it can be determined whether the pixels in the refocused image belong to the focused part or the non-focused interference part. Generally, $threshold_1$ takes three quarters of $C(x, y)$ and $threshold_2$ takes one quarter of $C(x, y)$.

$$I_{Trimap}(x, y) = \begin{cases} 0 & C(x, y) > threshold_1 \\ 1 & C(x, y) < threshold_2 \end{cases} \quad (7)$$

Where, $I_{Trimap}(x, y)$ represents the trimap marking at the pixel (x, y) . When $C(x, y)$ is higher than the threshold $threshold_1$, the value of $I_{Trimap}(x, y)$ is 0, indicating that the pixel (x, y) belongs to the non-focused interference part. On the contrary, when $C(x, y)$ is lower than the threshold $threshold_2$, the value of $I_{Trimap}(x, y)$ is 1, indicating that the pixel (x, y) belongs to the focused part. Those pixels that are not marked are uncertain regions, so equation (7) can automatically mark the trimap.

Fig. 6 shows the result of automatically marking the trimap of the refocused image. The white part belongs to focused area, the black part belongs to non-focused interference area, and the

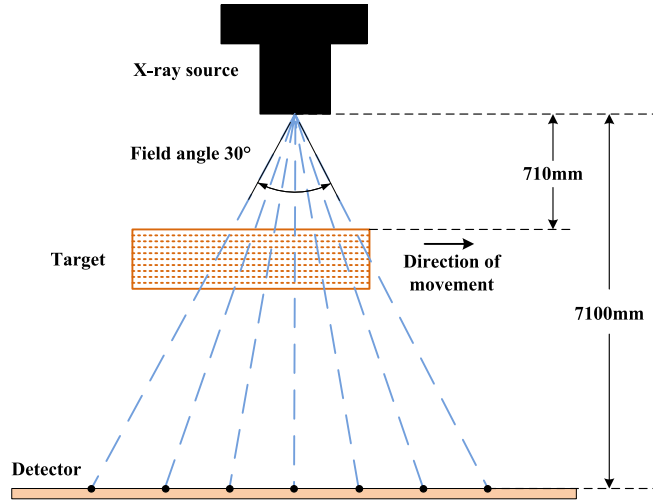


Fig. 7. The simulation imaging system model.

unmarked part is an uncertain area. Through this method, the trimap can be marked very well, which can solve the tedious problem of manual marking and facilitate the subsequent use of image segmentation matting method to separate the object and interference information.

Assuming that i is the pixel coordinate, T_i is the focused object, and O_i is the non-focused interference, according to the image matting method [18], the refocused image I_i is

$$I_i = \beta_i T_i + (1 - \beta_i) O_i \quad (8)$$

Meanwhile, equation (8) can be derived as

$$\beta_i = a I_i + b \quad \forall i \in w \quad (9)$$

where, $a = \frac{1}{T-O}$, $b = -\frac{O}{T-O}$, and w is a window centered on i . The cost function for β , a and b is

$$J(\beta, a, b) = \sum_{j \in I} \left(\sum_{i \in w_j} (\beta_i - a I_i - b)^2 + \varepsilon a_j^2 \right) \quad (10)$$

where, w_j is a window centered on j , and ε is a regularization term. The cost function for β can be calculated as

$$J(\beta) = \beta^T \cdot Lp \cdot \beta \quad (11)$$

where, Lp is a Laplacian matrices, which can be expressed as

$$\sum_{k(i,j) \in w_k} \left(\delta_{ij} - \frac{1}{|w_k|} \left(1 + \frac{1}{\frac{\varepsilon}{|w_k|} + \delta_k^2} (I_i - u_k)(I_j - u_k) \right) \right) \quad (12)$$

δ is the Kronecker symbol function, u_k and δ_k are the mean and variance of the pixels at the window of k . According to the image matting algorithm, the final clear imaging of objects at different depths can be obtained.

3.4 The Simulation Experiment

This section carried out a simulation experiment to verify the effectiveness of the X-ray layered refocusing imaging method. In the experimental system, the field of view angle is 30°, the distance between the ray source and the detector is 7100 mm, the distance between the front end of the

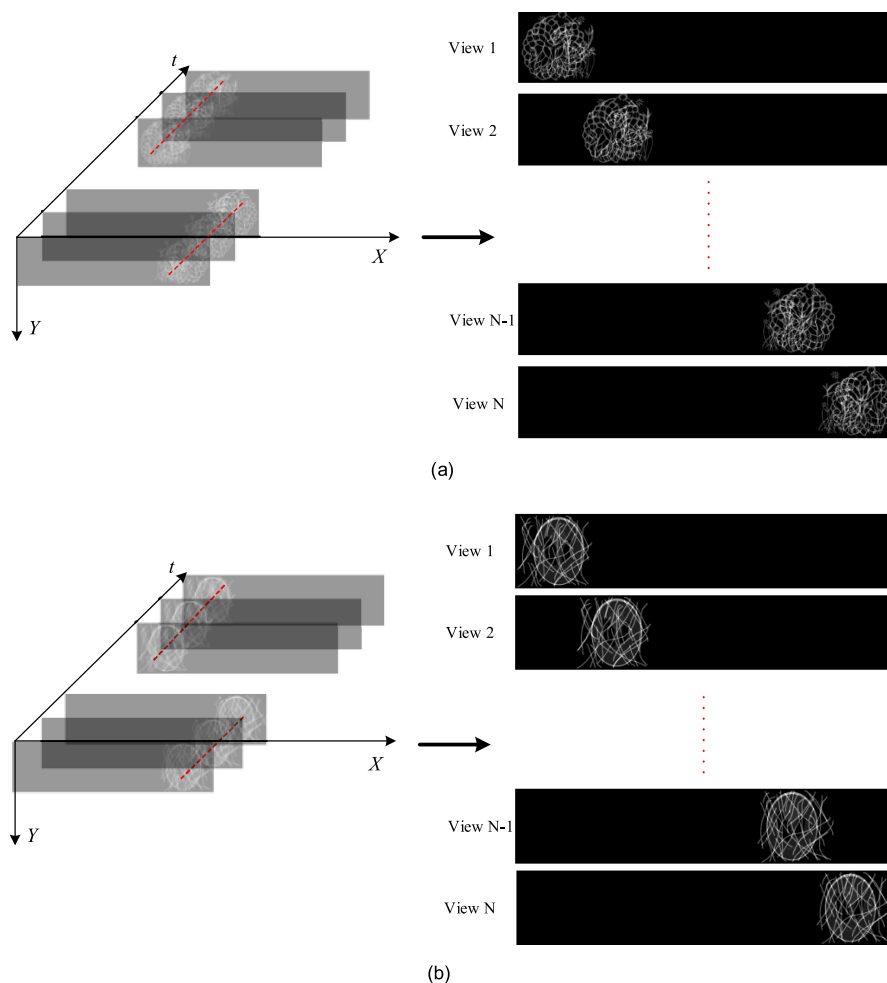


Fig. 8. The multi-view projection data of the two sets of multi-layer objects. (a) Multi-view image of messy wire and phantom model. (b) Multi-view image of multi-layer plants.

target and the ray source is 710 mm, and the pixel size of the detector is 1 mm. The simulation imaging system model is shown in Fig. 7.

This paper simulates two sets of multi-layer objects for experimental verification, the first group consists of two layers with messy wire and phantom model, the second group consists of three layers with different flowers and plants. The projection process carry out in accordance with radon transform, the multi-view projection data of the two sets of multi-layer objects are as follows.

According to the theory of refocusing imaging, the results of refocused imgs can be obtained as follows.

Refocus imaging is performed through the multi-view images, as shown in Fig. 9. The simulation experiment achieve refocusing images of the object at different depth layers and verifies the effectiveness of the X-ray layered refocusing imaging method.

Through the above analysis, it is easy to get the flowchart of the method proposed in this paper (see Fig. 10).

4. Experimental Result and Discussions

This section describes in detail the experiments conducted to verify the performance of the proposed method. The system is composed of an X-ray, plane array detector and a linear motion

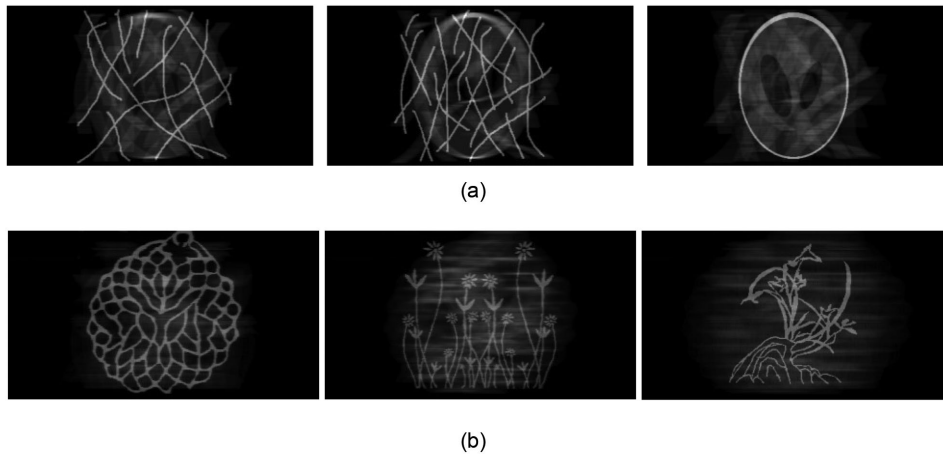


Fig. 9. Refocusing images of objects at different depths layers. (a) Messy wire and phantom model refocus result. (b) Multi-layer plants refocus result.

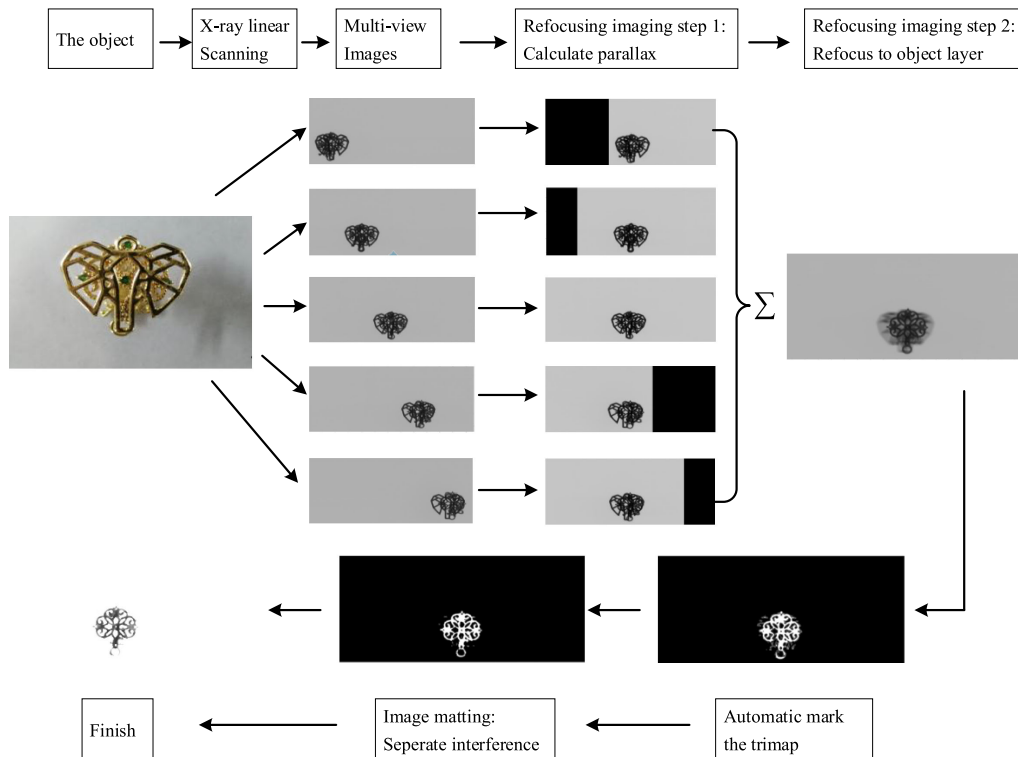


Fig. 10. Flowchart of X-ray layered refocusing imaging.

platform. The distance between the X-ray source and the moving platform is set to 142 mm, and the distance between the X-ray source and the detector is set to 1420 mm. the pixel size of the detector is 0.2 mm, and the stepping amplitude of the platform is set to 0.02 mm. The object is designed as a multilayer structure. In Section 4.1, the refocusing imaging experiment for different depth objects is designed to verify the feasibility of the proposed method. In Section 4.2, the refocusing imaging experiment for removing non-focused interference is designed to verify

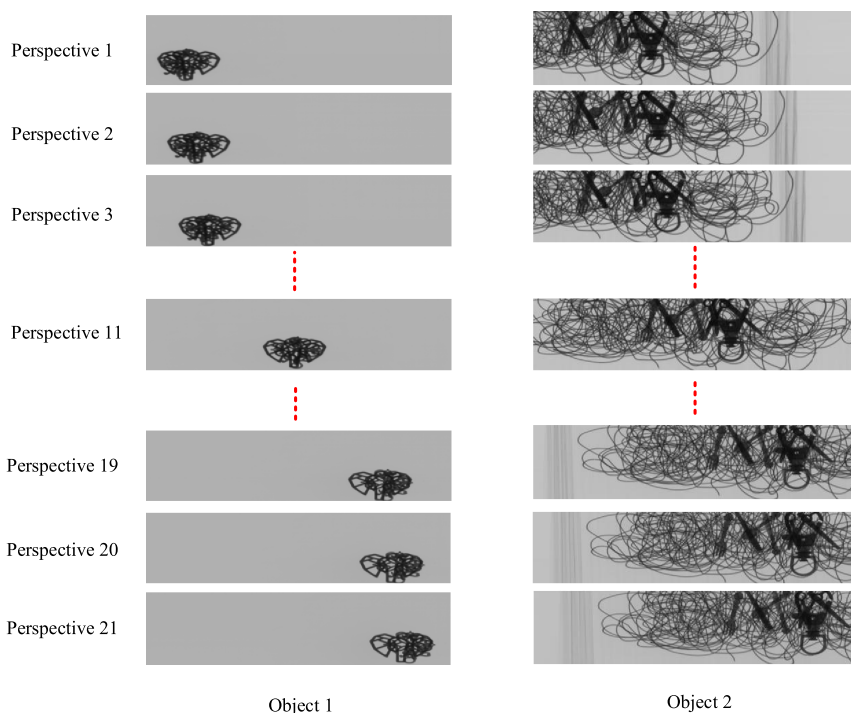


Fig. 11. Projection images from multiple perspectives.

the automatic marking matting algorithm can effectively remove the non-focused interference and improve the reconstructed image quality. In Section 4.3, the effects of different sampling rates on reconstruction quality were compared and analyzed.

4.1 Refocusing Imaging Experiment for Different Depth Objects

The object to be detected moves through the X-ray irradiation region in a straight line according to the above parameters, and then a series of X-ray photography images can be obtained. At a certain space interval (the sampling rate is 21), the corresponding projection images of multi-view can be obtained.

As shown in Fig. 11, the objects at different depths occlude each other, forming serious interference and affecting the detection and recognition of the objects at different depths layer. According to the refocusing imaging algorithm, the object at the specified depth layers can be reconstructed.

As shown in Fig. 12, the objects in the reconstruction image at the specified depth layers are enhanced, but the objects in the non-focused layer still form some interference in the image.

4.2 Refocusing Imaging Experiment for Removing Non-Focused Interference

According to the automatic marking matting algorithm of removing non-focused interference proposed in Section 3.3, objects at specific depth layers are clearly reconstructed. As shown in Fig. 13, interference in non-focused areas can be well suppressed. The object structure of the focused layer is basically complete and can be effectively detected and recognized.

4.3 Refocusing Imaging Experiment With Different Sampling Rates

During the process of refocusing imaging, the prerequisite of reconstructing a point is that at least one perspective can capture the information about the point without severe interference. Therefore,

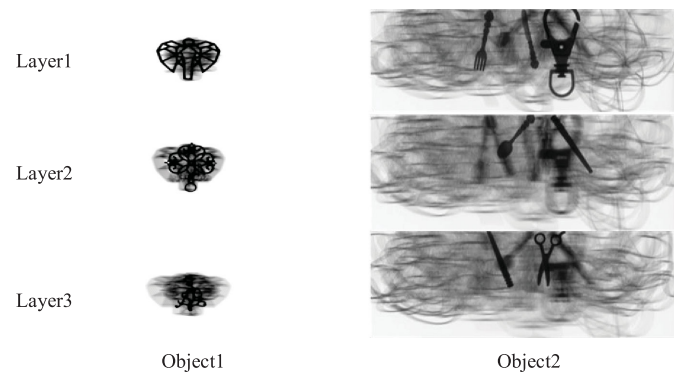


Fig. 12. Refocusing imaging results.

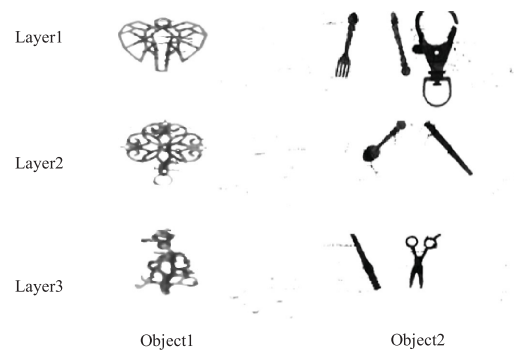


Fig. 13. Results of removing non-focused interference.

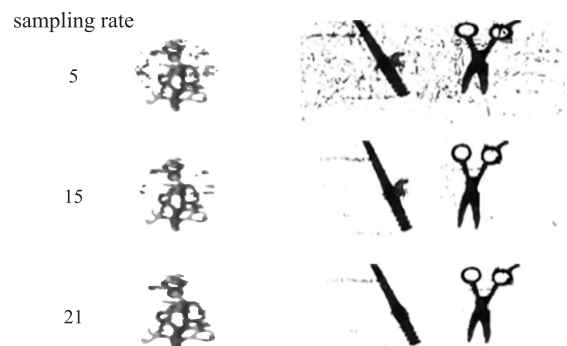


Fig. 14. Refocusing imaging result with different sampling rates.

the method in this paper is very sensitive to the spatial sampling interval. When the radiation angle of the X-ray source is fixed, the probability that object point is seriously disturbed increases with the increase of space sampling interval. Therefore, increasing the sampling rate is helpful to improve the quality of the reconstruction image. This experiment compares the quality of reconstructed images with different sampling rates at specific radiation angles, the result is shown in Fig. 14.

The Fig. 14 shows the reconstruction result of the objects with sampling rates of 5, 15 and 21, respectively. It can be seen that with the increase of the sampling rate, the structural information of the focused-layer object performed better, and the non-focused layer interference was also suppressed better.

5. Conclusion

For solving the information overlap during the object projection at different depths in X-ray digital imaging system, the X-ray refocusing layered imaging based on linear scanning is proposed. With the help of the refocusing imaging algorithm in the field of visible light and the automatic marking matting algorithm, the object structure information at specified focused-layer can be effective and clear reconstruct by rearranging the image sequence obtained from a simple linear scanning into multi-view projection images. The proposed method in this paper is similar to the layered tomography method of linear scanning, but it overcomes the difficulty of reconstruction caused by less information in three-dimensional Fourier space, and it can reconstruct the object at specified depth with less angled projection images. What's more, the key parameters affecting the reconstructed image quality are also analyzed, such as the view-angle sampling rate.

Further actions should be taken to modify the proposed method. Due to the limitation of the system's ray source views, the inter-layer resolution is relatively low, which cannot be directly used for the high-quality layered reconstruction with high layer density and overly complex structures. However, it might be solved by enlarging the detected area or increasing the ray sources to expand the effective system views, or by studying non-linear multi-view hierarchical reconstruction methods in the future.

References

- [1] J. Fu, B. H. Jiang, and B. Li, "Large field of view computed laminography with the asymmetric rotational scanning geometry," *Sci. China*, vol. 53, no. 8, pp. 2261–2271, 2010.
- [2] J. Fu, X. H. Hu, and H. Zhao, "New iterative reconstruction technique for large field of view digital tomosynthesis," *J. Med. Imag. Health Informat.*, vol. 4, no. 3, pp. 404–409, 2014.
- [3] D. P. Boyd, R. G. Gould, J. R. Quinn, R. Sparks, J. H. Stanley, and W. B. Herrmannsfeldt, "A proposed dynamic cardiac 3-D densitometer for early detection and evaluation of heart disease," *IEEE Trans. Nuclear Sci.*, vol. 26, no. 2, pp. 2724–2727, Apr. 1979.
- [4] J. M. Yue *et al.*, "Computed laminography and reconstruction algorithm," *Chin. Phys. C*, vol. 36, no. 8, pp. 777–783, 2012.
- [5] S. Gondrom and S. Schropfer, "Digital computed laminography and tomosynthesis functional principles and industrial applications," *Miscellaneous Workshops German Soc. NDT (DGZIP Workshops)*, vol. 7, no. 2, pp. 75–81, 1999.
- [6] M. Levoy and P. Hanrahan, "Light field rendering," in *Proc. Int. Conf. Comput. Graph. Interactive Techn.*, New York, NY, USA, 1996, pp. 31–42.
- [7] M. Levoy *et al.*, "Light field microscopy," *ACM Trans. Graph.*, vol. 25, no. 3, pp. 924–934, 2006.
- [8] Z.Y. Zhang and M. Levoy, "Wigner distributions and how they relate to the light field," in *Proc. Int. Conf. Comput. Photography*, San Francisco, CA, USA, Apr. 16/17, 2009, pp. 1–10.
- [9] K. Nagafune, S. Watanabe, and H. Shioya, "An evolutionary multi-criterion optimization approach utilizing the characteristics of strength distribution for sparse CT image reconstruction," in *Proc. Int. Symp. Soft Comput. Intell. Syst.*, Kyushu, Japan, Dec. 3-6, 2014, pp. 353–358.
- [10] D. R. Jiang, L. Li, Z. Q. Chen, G. Wang, and H. Gao, "Patch-wise non-local low-rank for few-view multi-energy CT reconstruction," in *Proc. IEEE Nuclear Sci. Symp. Med. Imag. Conf.*, Anaheim, USA, Oct. 27/Nov. 3, 2012, pp. 2407–2410.
- [11] K. Kim *et al.*, "Sparse-view spectral CT reconstruction using spectral patch-based low-rank penalty," *IEEE Trans. Med. Image*, vol. 34, no. 3, pp. 748–760, Mar. 2015.
- [12] F. Xu *et al.*, "Comparison of image quality in computed laminography and tomography," *Opt. Express*, vol. 20, no. 2, pp. 794–806, 2012.
- [13] J. M. Que *et al.*, "Computed laminography and reconstruction algorithm," *Chin. Phys. C*, vol. 36, no. 8, pp. 777–783, 2012.
- [14] V. Vaish, "Using plane+ parallax for calibrating dense camera arrays," in *Proc. IEEE Comput. Soc. Conf. Comput. Vision Pattern Recogn.*, Washington, DC, USA, Jun. 27/Jul. 2, 2004, pp. 2–9.
- [15] V. Vaish *et al.*, "Reconstructing occluded surfaces using synthetic apertures: Stereo, focus and robust measures," in *Proc. Comput. Vision Pattern Recogn.*, 2006, vol. 2, pp. 2331–2338.
- [16] B. Wilburn *et al.*, "High performance imaging using large camera arrays," *ACM Trans. Graph.*, vol. 24, no. 3, pp. 765–776, 2005.
- [17] P. Zhao, Y. N. Zhang, X. D. Chen, and Y. H. Yang, "Synthetic aperture imaging using pixel labeling via energy minimization," *Pattern Recogn.*, vol. 46, no. 2013, pp. 174–187, 2012.
- [18] J. Zhu, D. S. Zhang, and G. J. Lu, "An enhancement to closed-form method for natural image matting," in *Proc. Int. Conf. Digit. Image Comput.: Techn. Appl.*, Sydney, Australia, Dec. 1–3, 2010.